A key role for diffusion creep in eclogites: Omphacite deformation in the Zermatt-Saas Unit, Italian Alps

David D. McNamara[1] (d.mcnamara@liverpool.ac.uk)

John Wheeler[1] (j.wheeler@liverpool.ac.uk)

Mark Pearce[2] (Mark.Pearce@csiro.au)

David J. Prior[3] (david.prior@otago.ac.nz)

[1] University of Liverpool, Jane Herdman Building, 4 Brownlow Street, Liverpool, L69 3GP, UK

[2] CSIRO Mineral Resources, Clayton, Vic 3168, Australia

[3] University of Otago, Geology Department, 360 Leith Walk, Dunedin, 9054, New Zealand

Corresponding author: Dr David D. McNamara

This manuscript is paper is a non-peer reviewed preprint submitted to EarthArXiv. This manuscript has been submitted to the Journal of Structural Geology for review.

Abstract

Eclogites are important components of subduction-collision zones, with the mineral omphacite acting as the supporting framework mineral that accommodates the majority of any accumulated strain. As such it is important to determine which deformation mechanisms operate in omphacite during and after its formation to understand the rheology of deforming subducted crust. Such information is key to determining important information on the conditions, dynamics, and kinematics of subduction-collision tectonic regions. Using a combination of microanalytical techniques on eclogitic LS-tectonites from the Zermatt-Saas unit of the Italian Alps, we explore the mechanisms which resulted in both an omphacite shape and lattice preferred orientation. Omphacite defines both foliation and lineation in these rocks and a strong S-type lattice preferred orientation. Scarcity of microstructures associated with dislocation creep and sharp asymmetrical chemical zonation in omphacite grains suggest lattice preferred orientation formation via predominantly diffusion creep. Modelling of the P-T conditions possible for observed mineralogy and mineral geochemistry, and textural relationships between omphacite and retrogressive minerals, place the action of diffusion creep, at the latest, by the onset of retrogression of these Zermatt-Saas eclogites. We propose a model of eclogite deformation that occurred initially via small amounts of dislocation creep which moved quickly into a dominant diffusion creep field, particularly as exhumation/retrogression of these eclogite rocks began. This result suggests that diffusion creep can dominate eclogite deformation at high P-T conditions in subduction zones.

1 Introduction

Microstructural investigation of deformation processes is key to establishing the kinematics, dynamics, and rheology of deformed rocks (Blenkinsop 2002). Bulk rock strength is governed by which deformation mechanisms are active, and these mechanisms must be determined from rock and mineral microstructure. The relative contribution of different deformation mechanisms to the total observed strain is strongly dependent on the deformation conditions (pressure, temperature, strain rates), mineralogy, and grain sizes, all of which vary with time (White 1976; Karato and Jung 2003; Rybacki and Dresen 2004; Warren and Hirth 2006). This has led to the use of deformation mechanism maps as tools for monomineralic rocks that can inform on a rocks pressure and temperature deformation pathway (Ashby 1972; Knipe 1989), especially when coupled with an understanding of evolving mineralogy in metamorphic rocks.

Eclogites are medium-temperature, high to ultra-high pressure, metamorphic rocks which occur in the upper mantle, and in subduction and collision zones. As such, the mechanisms by which these rocks deform is crucial to understanding the tectonics of these important geological locales (Philippot and Roermund 1992; Jin et al. 2001). Geodynamic models of the thermo-mechanical processes occurring in subduction and exhumation are based on the rheological properties of eclogitic rocks (Kurz et al. 2004; Burov et al. 2014), eclogite flow strength is used to impose upper bounds on shear stress across plate boundaries deep in subduction zones (Piepenbreier and Stöckhert 2001), and eclogitization of mafic lower crust, and the associated increase in density, is thought to contribute to the recycling of this material into the mantle as well as helping drive plate convergence (Doin and Henry 2001).

Omphacite and garnet are two main mineral constituents of eclogite facies rocks. In most eclogites, omphacite is the framework supporting mineral with garnet usually occurring as isolated porphyroblasts. It is commonly observed that garnet acted as a rigid body during eclogite deformation, though this is not always the case (Prior et al. 2002; Mainprice et al. 2004; Storey and Prior 2005; Zhang and Green 2007). Omphacite, the dominant phase in eclogite facies

rocks, accommodates strain and controls the rheology of eclogites, deforming plastically (Godard and Roermund 1995; Zhang et al. 2006; Keppler 2018), In addition to omphacite and garnet, eclogite facies rocks can also host a range of other minerals which can show varying degrees of plastic deformation e.g. phengite, quartz, rutile, and epidote minerals, and are thought to contribute to eclogite rheological properties depending on mineral abundance (Mauler et al. 2001; Keppler 2018; Park and Jung 2019).

This study characterises the deformation mechanisms operating in omphacite from deformed eclogite facies rocks of the Zermatt-Saas Unit from Punta Telcio, Northwest Italy using a combined microchemical and microstructural approach. By determining the deformation processes responsible for omphacite deformation in the Zermaat-Saas eclogite rocks we aim to provide new insight into how eclogites deformed during the subduction conditions responsible for the closure of the Iapetus Ocean which eventually led to the formation of the European Alps.

1.1 Review of Omphacite Microstructure and Deformation Mechanisms with Respect of LPO formation

Deformation mechanisms maps are available for a number of minerals (quartz, calcite, galena, etc.; (White 1976; Atkinson 1977; Ranalli 1982; Tsenn and Carter 1987; Drury et al. 1989) but a complete deformation mechanism map for omphacite has yet to be developed. Aspects have been experimentally constrained (Zhang et al. 2006; Moghadam et al. 2010) and often diopside (the calcic omphacite endmember) deformation mechanisms maps are utilised as proxies (Bascou et al. 2002). Omphacite often forms a foliation and lineation within deformed eclogites with grains typically having a shape preferred orientation (SPO).

Lattice preferred orientations (LPO) are common in deformed omphacite (Helmstaedt et al. 1972; Godard and Roermund 1995; Ulrich and Mainprice 2004; Rehman et al. 2023), though debate continues as to which deformation mechanisms are responsible for its creation. Omphacite LPO has been

reported to form from twinning (Godard and Roermund 1995; Trepmann and Stöckhert 2001; Brenker et al. 2002), though this is rarely observed in terrestrial rocks (Trepmann and Stöckhert 2001), and so is thought to only occur at low temperatures and very high strain rates.

LPO formation in deformed omphacite is usually attributed to the action of dislocation creep and complimentary processes such as grain boundary migration and subgrain rotation recrystallisation (Buatier et al. 1991; Philippot and Roermund 1992; Godard and Roermund 1995; Bascou et al. 2002; Kurz et al. 2004; Keppler et al. 2016). Commonly documented omphacite microstructures include undulose extinction, deformation twinning, sub-grains, lattice preferred orientations, and exsolution lamellae (Buatier et al. 1991; Ábalos 1997; Bascou et al. 2001; Mauler et al. 2001; Brenker et al. 2002; Foreman 2004; Zhang et al. 2006). Transmission electron microscopy (TEM) of omphacite reveals microstructures such as dislocations and dislocation networks, tilt walls, (100) microtwins, (010) planar faults, chain multiplicity faults, stacking faults, and antiphase domains, the latter of which results from atomic ordering in omphacite (changing space group from C2/c, or a metastable version of C2/c, to P2/n) (Roermund and Boland 1981; Buatier et al. 1991; Philippot and Roermund 1992; Godard and Roermund 1995; Brenker et al. 2002, 2003; Müller et al. 2004, 2011). TEM identifies common slip systems in omphacite to include [001](100), [001]{110} and ½<110>{110} (Roermund and Boland 1981; Roermund 1984; Godard and Roermund 1995), and occurrences of chain multiplicity faults (CMFs) parallel to (010) in omphacite suggest that ½[011](010) may also be an important slip system in omphacite (Müller et al. 2004). While there is plenty of microstructural evidence that dislocation creep is active in deformed omphacite, problems exist with diagnosing it as the sole LPO forming mechanism.

Models for LPO formation via dislocation creep fall between two end-member classifications; the single slip and multiple slip models (Wenk and Christie 1991). The single slip model, applied to dislocation creep in omphacite due to its low crystal symmetry (Mainprice and Nicolas 1989), requires the slip systems [001](100) and [001](010), the ‘easiest’ slip systems in clinopyroxene,

to be dominant. While the [001](100) slip system is commonly observed in naturally deformed omphacite, the [001](010) slip system is rarely recorded (Godard and Roermund 1995). Applying the multiple slip model to omphacite is also problematic. Only three commonly observed active slip systems are noted in naturally and experimentally deformed omphacite thus failing to meet the von Mises criterion for five independent slip systems. This is related to the fact that none of the three slip systems intersect the tetrahedron chains and thus, for some crystallographic orientations, deformation cannot be accommodated by slip and another process must be in operation (Godard and Roermund 1995). Furthermore, a multiple slip model assumes homogeneous deformation across the rock containing the omphacite and as mentioned, garnet commonly behaves rigidly in eclogites. Alternatively, use of viscoplastic-self-consistent (VPSC) models suggests that omphacite LPO can be formed purely from dislocation creep (Bascou et al. 2002; Ulrich and Mainprice 2004). VPSC models reproduce typical omphacite LPOs from naturally deformed eclogites and results show that patterns developed can be directly produced by dislocation creep occurring mainly on the 1/2<110>{$\bar{1}$10}, [001]{110} and [001](100) systems, with others contributing to a much lesser extent.

Finally, the operation of DMT mechanisms (diffusion creep, dissolution-precipitation, etc.) in eclogite is also proposed as a mechanism for the formation of omphacite LPOs in deformed eclogites. DMTs are evidenced by omphacite growth in garnet cracks (Erambert and Austrheim 1993), overgrowth of strained omphacite crystals (Godard and Roermund 1995), and syntectonic omphacite vein growth (Essene and Fyfe 1967; Carpenter 1979; Philippot 1987). DMTs are used to explain omphacite pressure shadows around garnet porphyroblasts indicating omphacite growth is sensitive to local changes in stress orientation (Godard and Roermund 1995; Mauler et al. 2001). Grain growth can result in LPO development in a mineral via the selective growth of some grains and the elimination of others (anisotropic dissolution-precipitation). Indeed, chemical zonation is commonly observed in omphacite from deformed eclogites, with oscillatory and discontinuous, concentric zonation patterns described, microscale patterns that can suggest the action of preferred growth mechanisms during eclogite deformation (Carpenter 1982; Piepenbreier and

Stöckhert 2001; Kurz et al. 2004; Keppler et al. 2016). Some omphacite LPO studies (Cao et al. 2021; Rogowitz and Huet 2021) have found that in many deformed eclogites, a strong omphacite LPO can develop made of omphacite grains that show little evidence of crystal plasticity (e.g. undulating extinction, low amounts of intracrystalline misorientations >2°, few subgrain boundaries). This observation combined with observed omphacite grain chemical zonation in these studies suggests a DMT process is most likely the main mechanism for LPO development. Observations of omphacite chemical zonation patterns combined with scarcity of intragrain deformation features are noted in deformed eclogites from the Tauern Window in the European Alps and is suggested as an indication of diffusion creep action here (Stünitz et al. 2020).

In monoclinic pyroxenes, calculated attachment energies suggest that face growth rates are greatest for [010], intermediate for [100] and smallest for [001] and dissolution rates show the opposite (Panhuys-Sigler and Hartman 1981). Therefore, grains with [001] parallel to the least principal stress direction will grow faster than other grains and those with [010] parallel to the maximum principal stress direction will dissolve slower, favouring the perpetuation of omphacite crystals with orientations compatible with observed LPO patterns in deformed eclogites and omphacite filled veins (Godard and Roermund 1995). (Mauler et al. 2001) suggest that anisotropic growth and dissolution, rate controlled by grain boundary diffusion, explain the formation of omphacite LPO in the Vendée eclogites. Here omphacite crystal growth during deformation is evidenced by variation in crystal size between weakly and strongly deformed zones around a rigid garnet. Observed SPO and LPO patterns in these zones cannot be explained by dislocation creep (and lack expected dislocation associated microstructure), whereas oriented growth in an anisotropic stress field can.

DMT deformation mechanisms are grain size sensitive; as grain size increases the length of diffusion pathways increase and potential dissolution and precipitation sites decrease, thus flux decreases. However, eclogites examined by (Mauler et al. 2001) show that omphacite reaching grain sizes of >7 mm still shows evidence for diffusion creep suggesting the domain of geological

conditions in which diffusion processes are active is wider than expected. Diffusion creep has also been put forward as an omphacite LPO generating mechanism in lower temperature eclogite conditions, since unrealistic stresses and strain rates are required to form the LPOs from dislocation creep at these conditions (Godard and Roermund 1995).

Given the discussion of omphacite LPO formation above, the existing consensus is omphacite LPOs form from dislocation creep working in tandem with DMT mechanisms such as diffusion creep and preferential crystal growth (Helmstaedt et al. 1972; Godard and Roermund 1995; Mauler et al. 2001). In this study, to explore omphacite LPO formation via a combined mechanism process, we examine the microstructure and microchemistry of deformed omphacite in eclogites from the Zermatt-Saas unit in the European Alps.

1.2 Geological Setting and Sample Description

The eclogite facies rocks investigated in this study were obtained from Zermatt-Saas Unit outcrops at Punta Telcio, Valle De Gressoney, Italy (Figure 1). The Zermatt-Saas Unit is an ophiolitic layer of Late Jurassic, oceanic lithosphere obducted during the Alpine Orogeny (Amato et al. 1999). This unit underwent high-pressure metamorphism (~2-3 GPa) at temperatures of ~550-600 °C about 41-48 Ma (Barnicoat and Fry 1986; Lapen et al. 2003; Bucher 2005) and was exhumed from depth by the extensional Gressoney Shear Zone (GSZ) and erosion (Reddy et al. 1999). The geology of the Punta Telcio region, and the petrography and metamorphic evolution of the Zermatt-Saas eclogite facies rocks studies here, is detailed in (McNamara 2012) and (McNamara et al. 2012) and only covered here briefly paying specific attention to the omphacite crystals in these rocks.

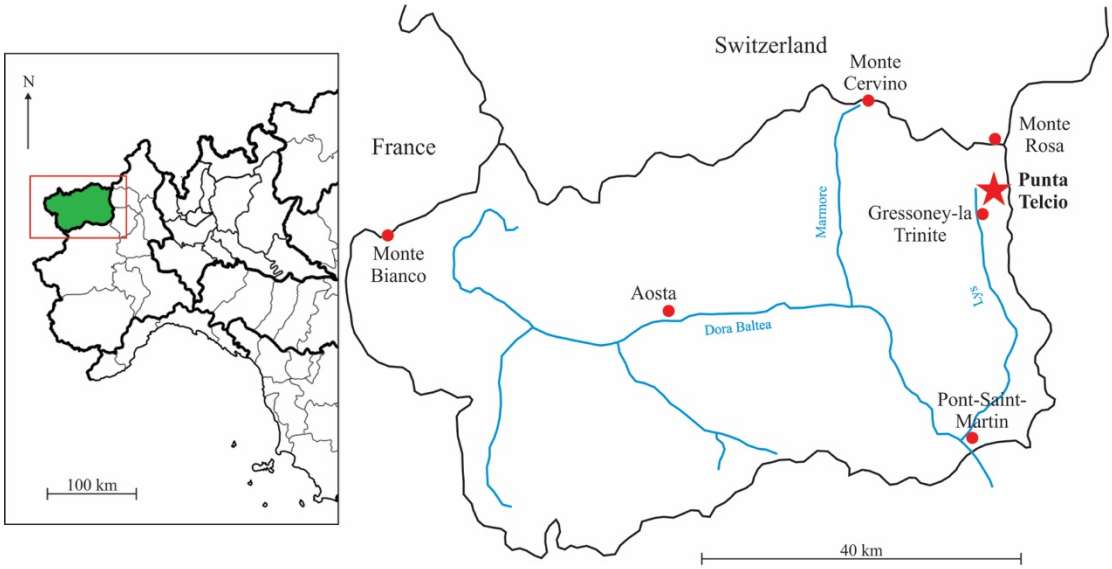

Figure 1. Location map of Punta Telcio (red star) in the Valle d'Aosta region of Italy (black lines are borders, blue lines are rivers) where eclogite samples for this study were collected. Inset shows the region's location in NW Italy on the Italian-French-Swiss border.

The eclogite facies rocks of the Zermatt-Saas Unit at Punta Telcio are predominantly composed of pale green omphacite, garnet, clinozoisite, white mica (phengite), quartz, and accessory rutile. Omphacite defines a strong shape fabric foliation and weak lineation (S-tectonite) in these rocks (Figure 2). Omphacite grain sizes (measured on grain long axes) are approximately between 200 and 500 μm and most grains have a hornblende-albite symplectite rim of variable width (<100-200 μm) (Figure 2). Omphacite can also be found as inclusions within garnet grains. Light microscopy reveals some individual omphacite grains have variable birefringence (possible subgrains) and undulose extinction (Figure 2). Garnet grains have porphyroblastic or atoll forms with grain sizes up to 3 mm and are all wrapped by the omphacite foliation (Figure 2). The eclogites in this study area are also variably overprinted by an initial blueshcist facies event followed by a greenschist facies event (McNamara et al. 2012). Glaucophane and clinozoisite associated with retrogression of the eclogite peak assemblage can be texturally found both as consistent with the omphacite foliation, suggesting deformation during the onset of retrogression,

and cross-cutting the omphacite foliation, suggesting a static growth phase of retrogression as discussed in (McNamara et al. 2012).

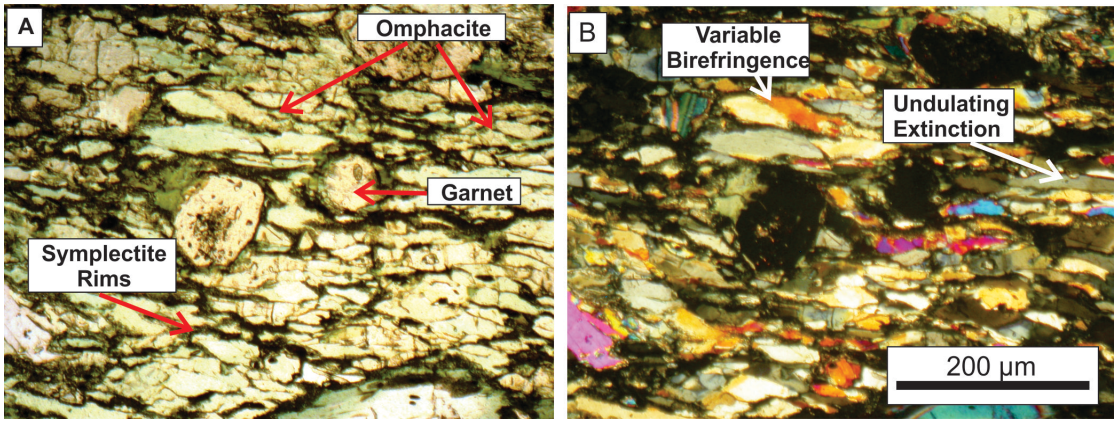

Figure 2. Photomicrographs of eclogite from Punta Telcio (sample S6.8) showing omphacite forming an SPO that wraps garnet grains. Omphacite grains have symplectite rims, variable birefringence and undulating extinction. A) Plane polarised light, B) Crossed polarised light.

2 Methods

2.1 Electron Backscatter Diffraction

Electron backscatter diffraction was utilised in this study to identify and characterise omphacite LPOs in the sampled eclogites, and to map grain-scale crystallographic deformation features such as sub-grain formation. Zermatt-Saas eclogite samples were thin sectioned perpendicular to foliation and parallel to lineation. Samples were prepared for electron backscatter diffraction (EBSD) by polishing them on a polyurethane lap for ~2.5-3 hours using a suspension of 0.05µm colloidal silicon (SYTON™) to remove residual surface damage and topography to optimise EBSD data collection (Prior et al. 1999). Samples were then thinly carbon coated to minimise charging effects while maintaining diffraction pattern intensity (Prior et al. 1996).

All crystallographic orientation data was collected by EBSD at the University of Liverpool using a CamScan X500 crystal probe scanning electron microscope (SEM) equipped with a thermionic field emission gun and a FASTRACK stage. A beam current of ~45-50nA and an accelerating voltage of 20kV were used for data acquisition. An angular resolution of ~1° is associated with this

technique with a spatial resolution of ~0.1μm. Data were collected using two methods; 1) combining a rectangular array of EBSD maps (step size of 1.5-3μm) together to provide crystallographic and microstructural information from a selected region of the thin sections (different measurement points are reached by moving the electron beam), and 2) use of the FASTRACK stage to collect data on a rectangular grid using a set step-size spacing of 300 - 350μm (thus different measurement points are reached by moving the sample mounting stage) (Prior et al. 2002) to provide bulk LPO data for each thin section. Electron backscatter patterns (EBSP) were indexed using the software package CHANNEL+ v5 from Oxford Instruments Ltd. Initial processing on beam maps and stage maps (with ≤10μm step size) removed isolated points where the orientation or phase differed from the neighbour points (wild spikes). Non-indexed points with >6 neighbouring indexed points were interpolated using an average of the neighbouring crystal phase lattice orientations (Prior et al. 2009). Misorientation distribution analyses is performed on omphacite EBSD maps (acquired using method 1 described above) to gain insight into potential microstructural processes that contribute to omphacite deformation, e.g., subgrain rotation recrystallisation by crystal plastic processes (Wheeler et al. 2001). Boundary misorientation function (BMF) analysis, for 2°-5° and 5°-10° subgrain misorientation boundaries, is performed following the method outlined in Rehman et al. (2023).

2.2 Transmission Electron Microscopy (TEM)

TEM investigation of omphacite was carried out to determine the presence of omphacite microstructures (e.g. dislocations, antiphase domains), and determine the ordering of the omphacite in these samples. TEM was performed at the Institute of Applied Geosciences at Technische Universität Darmstadt using a Philips CM12 transmission electron microscope operated at 120kV and equipped with an EDAX Genesis 2000 energy dispersive X-ray spectrometer. Samples were prepared from thin sections that had undergone EBSD. Specimens ~3mm in diameter are ultrasonically drilled from the uncovered thin section and glued to Mo grids using CRYSTALBOND glue. These are made suitable for TEM by Ar^+ ion milling using a GATAN Duo Mill.

343

344 ## 2.3 Geochemistry

345 Energy Dispersive X-ray spectroscopy (EDX) chemical maps and semi-
346 quantitative chemical analyses (using EDX counts calibrated against a known
347 Co standard) were determined using a CamScan X500 SEM at Liverpool
348 University. This SEM is equipped with an Oxford Instruments Ltd. INCA EDX
349 system with a 10mm^2 detection area, lithium drifted silicon (LiSi) detector, and
350 a beryllium window. Precise quantitative chemical data were gathered using
351 the Cameca SX 100 Electron Microprobe equipment at the University of
352 Manchester. Quantitative data are recalculated for Fe^{3+} using the stoichiometric
353 method of (Droop 1987).
354
355 Bulk rock composition is required for thermodynamic pseudosection modelling
356 and was determined by combining two data sets. Modal abundances of each
357 mineral phase were determined from a whole thin section map (eclogite sample
358 S6.8) using a Tescan Integrated Mineral Analyser (TIMA), Tescan MIRA SEM
359 equipped with 3 PulseTor energy dispersive X-ray (EDX) spectrometers
360 operating at 25 keV, and with a step size of 10 μm, and 2). This technique
361 allows the EDS detectors to count EDX elemental spectra from which is
362 performs mineral identification (Hrstka et al. 2018). Mean compositions of each
363 phase within the eclogites examined in this study was obtained from
364 quantitative EDX measurements made using the same microscope at 15 keV,
365 1.9 nA and using an Oxford Instruments X-Max^N 80mm^2 EDX detector with
366 beam calibration using a Co standard. For zoned phases, an attempt was made
367 to ensure that the number of EDX measurements of each composition was
368 representative of the volumetric variations in mineral composition (e.g. by
369 measuring transects). The rock bulk composition was then calculated by
370 summing the mean compositions of each phase weighted by their modal
371 abundances. This technique has an advantage over XRF such that phases
372 which cannot be modelled are not included in the bulk composition (apatite,
373 carbonates, sulphides) and no assumptions are required to correct from a
374 measured bulk composition e.g., removing Ca from XRF determination due to
375 apatite.

2.4 Phase Equilibrium Modelling

To constrain the evolution of metamorphic conditions for the Punta Telcio eclogites we used THERMOCALC to predict the equilibrium mineralogy expected as a function of P and T for a particular bulk composition. The bulk composition modelled is in the system NCKFMASHTO; we used THERMOCALC 3.4, dataset ds55 and the following activity composition models; clinoamphiboles (Diener et al. 2007), clinopyroxene (Green et al. 2007), garnet (White et al. 2007), chlorite (Holland et al. 1998), muscovite/paragonite (Coggon and Holland 2002), biotite (White et al. 2007), plagioclase (Holland and Powell 2003), and Ilmenite (White et al. 2000). The peak pressure conditions were identified using the identified mineral assemblages and using mineral chemical compositions to further constrain the conditions within that field. Mineral zoning present in the rocks is used to inform P-T-t paths using changes in mineral composition and abundance to compare to zoning patterns in the rocks. The modelled compositions and modal abundances were calculated using TCInvestigator v2.3 (Pearce et al. 2015).

3 Results

3.1 Microstructure

3.1.1 Omphacite LPO

Omphacite LPO patterns and their LS index values (Ulrich and Mainprice 2004) are presented in Figure 3 and Table 1. Punta Telcio eclogites present S-type LPO patterns (point maximum of <010> poles normal to the foliation and the <001> poles are dispersed in a girdle pattern within the foliation plane) with LS-Index values ranging between 0.108-0.307. No relationship is observed between omphacite grain size and LS index value.

Sample Number	Average Omphacite Grain Size (μm)	FASTRACK Step Size (μm)	Number of Omphacite Data Points	LPO Type	LS-Index Value	Grid Reference
S5.2	150	300	303	S-type	0.234	0409729 / 5080406
S5.6	300	400	251	S-type	0.211	0410214 / 5080792
S6.3	350	350	492	S-type	0.307	0410118 / 5080630
S6.4	300	350	726	S-type	0.122	0410118 / 5080630
S6.5	300	400	556	S-type	0.187	0410118 / 5080630
S6.7	150	300	121	S-type	0.262	0410283 / 5080532
S6.8	200	350	268	S-type	0.29	0410253 / 5080531
S6.12	250	350	226	S-type	0.219	0410169 / 5080527
S6.13	250	300	594	S-type	0.18	0410453 / 5080531
S6.14	200	300	322	S-type	0.136	0410158 / 5080529
S6.16	300	350	328	S-type	0.277	0410194 / 5055525
S6.18	250	400	387	S-type	0.234	0410182 / 5080472
S6.19	250	300	741	S-type	0.248	0410225 / 5080463
S6.22	100	300	705	S-type	0.108	0410233 / 5080420
S3-50B	200	350	510	S-type	0.218	Unrecorded reference

Table 1 Table of approximate omphacite grain sizes, FASTRACK step sizes used for LPO data acquisition, number of omphacite crystal lattice orientation measurements used to determine LPO, LPO type, and LS-index values, for each sample of deformed eclogite investigated from Punta Telcio in this study eclogites (grid reference using European 1950 map datum.

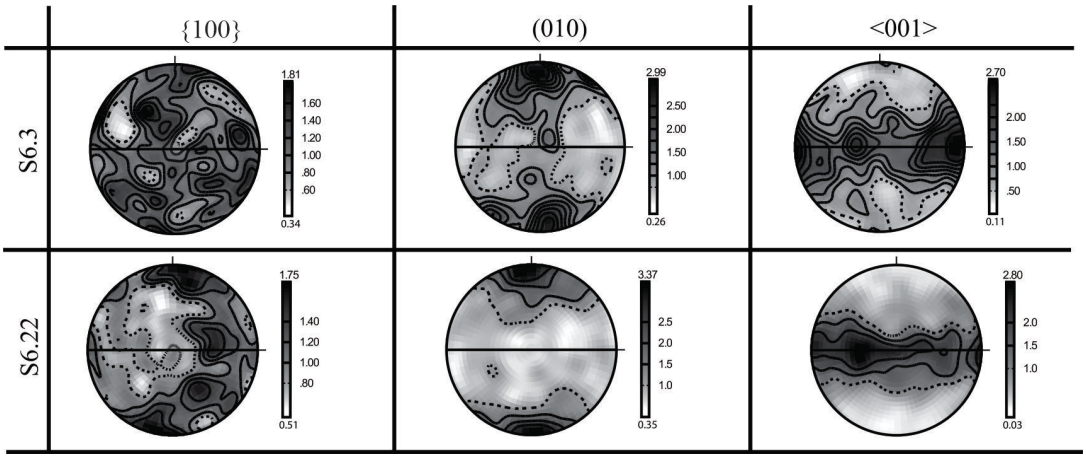

Figure 3. Omphacite pole figures of eclogite samples S6.3 and S6.22. S6.3 represents the least S-type LPO and S6.22 the most S-type LPO (see Table 1).

3.1.2 Omphacite Microstructure

Misorientation distribution analyses on EBSD grain maps of eclogite samples shows that between 10-20% of all omphacite neighbour pair pixels have low angle misorientations (<10-2°; Figure 4). Grain boundary maps of omphacite show that few grains contain distinct sub-grain boundaries (defined here as internal omphacite grain boundaries with misorientations of <10-2° across them) (Figure 5). TEM investigations reveal that omphacite grains contain a range of microstructures including dislocations and antiphase domains (Figure 6), while subgrain boundaries are not observed in TEM, supporting their infrequent appearance on EBSD grain boundary maps (Figure 5). Both C2/c and P2/n space group omphacite is observed in TEM, though the disordered P2/n version is dominant.

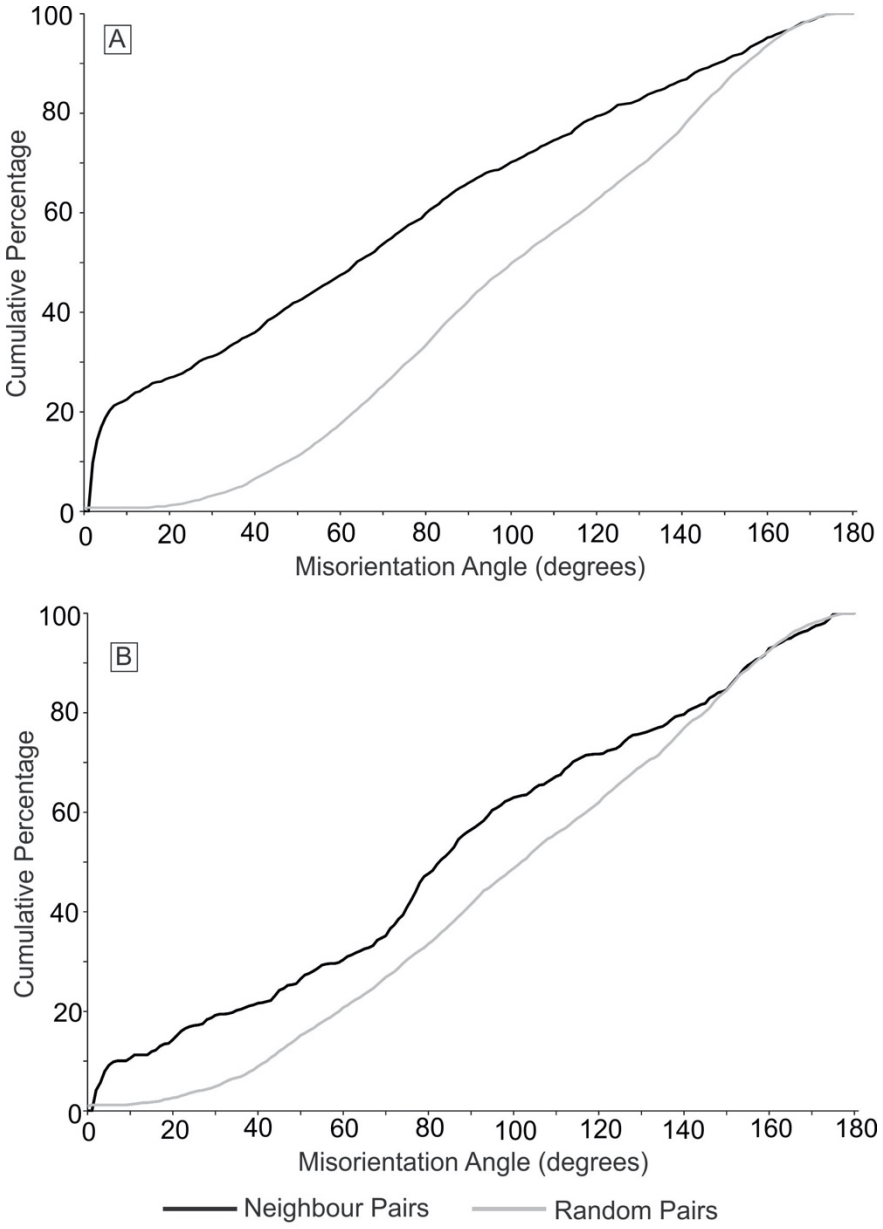

Figure 4. Cumulative misorientation distribution graphs for A) sample S6.4 and B) sample S6.8.

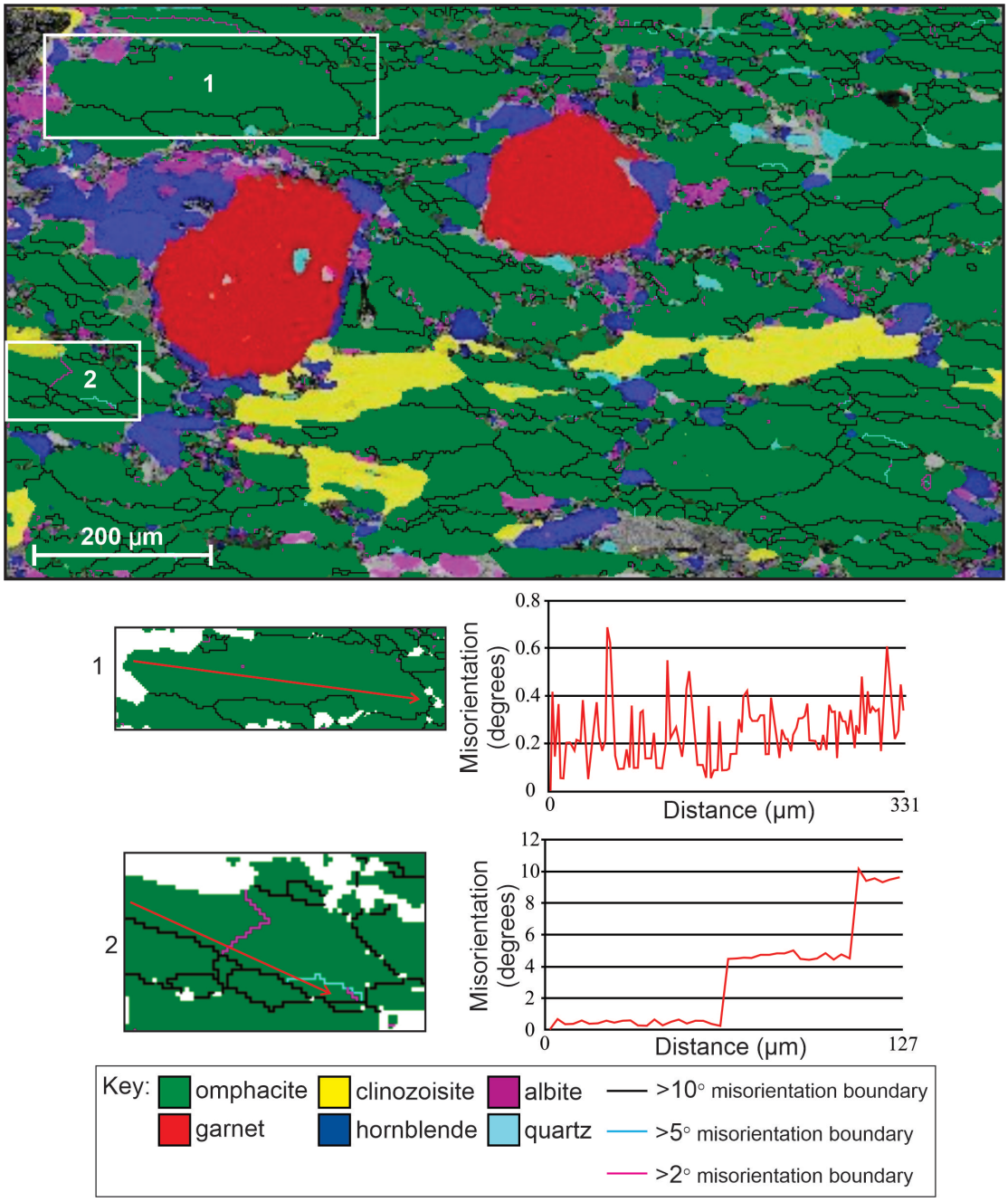

Figure 5. EBSD map (coloured for phase ID) with omphacite grain boundaries and subgrain boundaries (sample 6.8). Insets 1 and 2 represent individual grains and misorientation profile graphs (red arrows mark the location and direction of misorientation profiles).

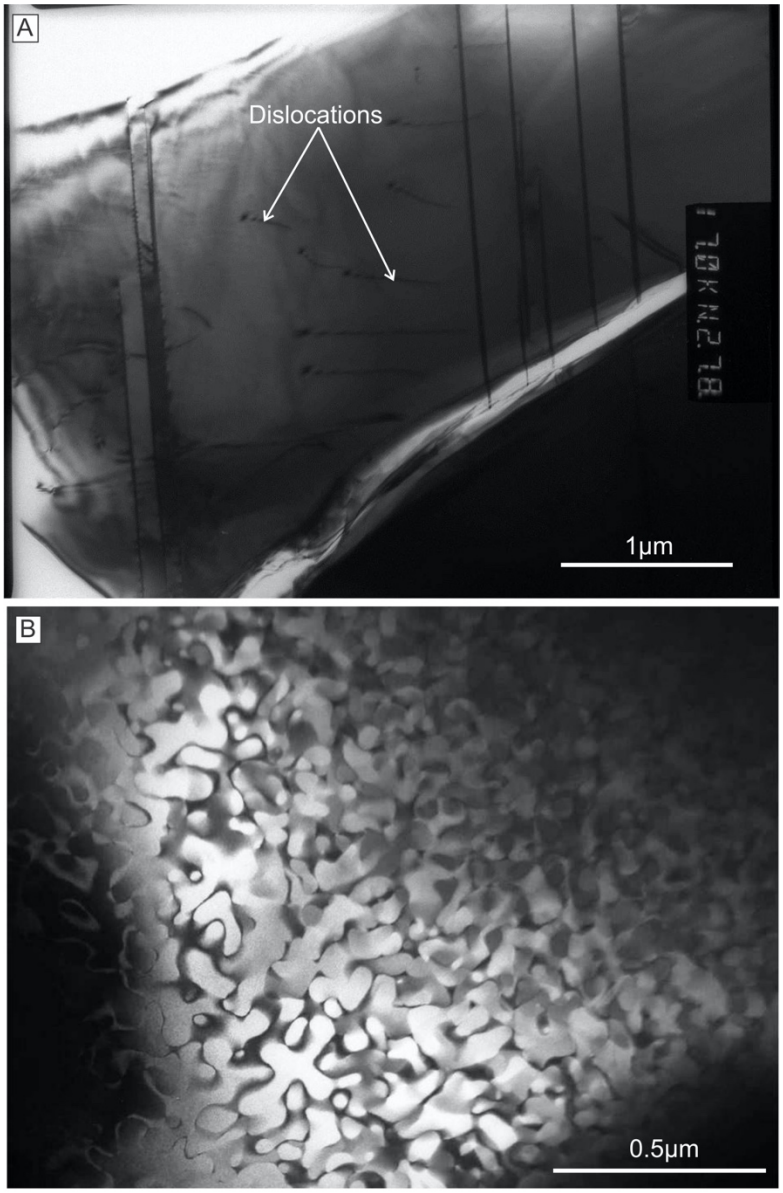

Figure 6. A) Dark field photomicrograph showing dislocations in an omphacite grain (sample S6.4). B) Dark field photomicrograph of antiphase domains in P2/n omphacite (sample S6.4).

BMF analysis of 2°-5° and 5°-10° subgrain misorientation boundaries in omphacite in deformed eclogites (Figure 7) reveals clustered misorientation axes around [001], (100), (106), (221) and (110) potentially indicating the action of the [001](100), [001]{110} and ½<110>{110} slip systems in omphacite here. No consistent BMF clustering patterns are observed for omphacite across all samples investigated.

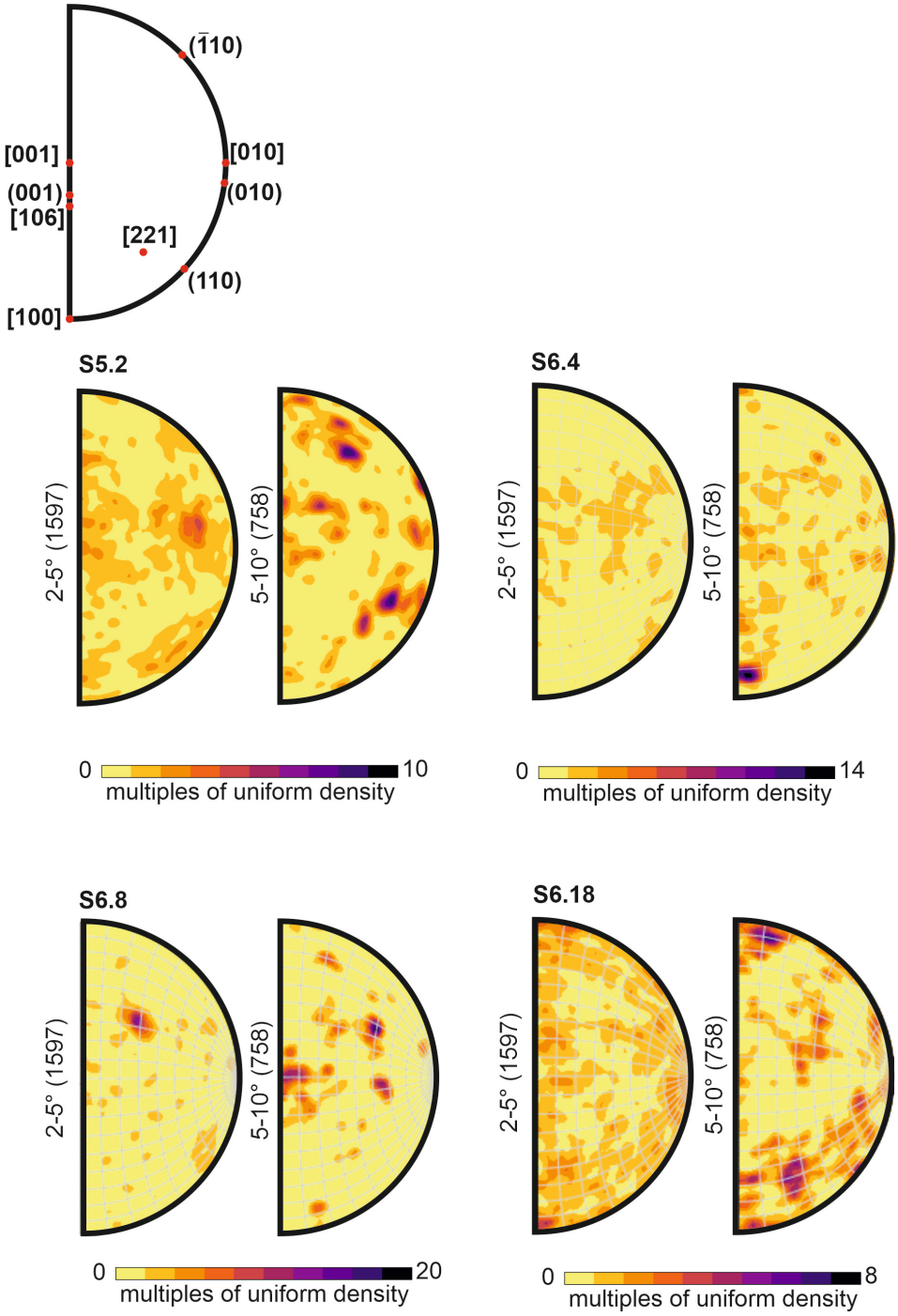

Figure 7. BMF analysis of omphacite subgrain misorientations from Punta Telcio deformed eclogites for samples S5.2, S6.4, S6.8, and S6.18.

3.2 Omphacite Geochemistry

Chemistry obtained from EMPA analyses determines the grains as 'omphacite' according to the classification set out by (Clarke and Papike 1968). Chemical mapping shows zonation in omphacite grains with sharp zonation boundaries (Figure 8; 9). Quantitative chemical measurements and mapping show that the

main zonation is due to varying amounts of Fe^{3+}, Ca, Na, Al, and Mg (Figure 8; 9; 10). Decreases in Na and Fe^{3+}, coincide with increases in Ca, Mg, and to a lesser extent Al. A key feature is that zonation is not concentric but occurs preferentially along the long axes of the omphacite grains and seems to occur either in both directions of the grain's long axes so that a symmetrical to near-symmetrical zonation pattern is achieved (Figure 8) or in one direction (from one side of the grain to the other (Figure 9). In those grains that show symmetrical to near-symmetrical zonation, the aegirine (Ae) content of the grain decreases from the core to rim. Additionally, the jadeite (Jd) component decreases slightly towards the grain edges with an increase in Fe-Ca-Mg pyroxene (augite/diopside) component (Figure 10).

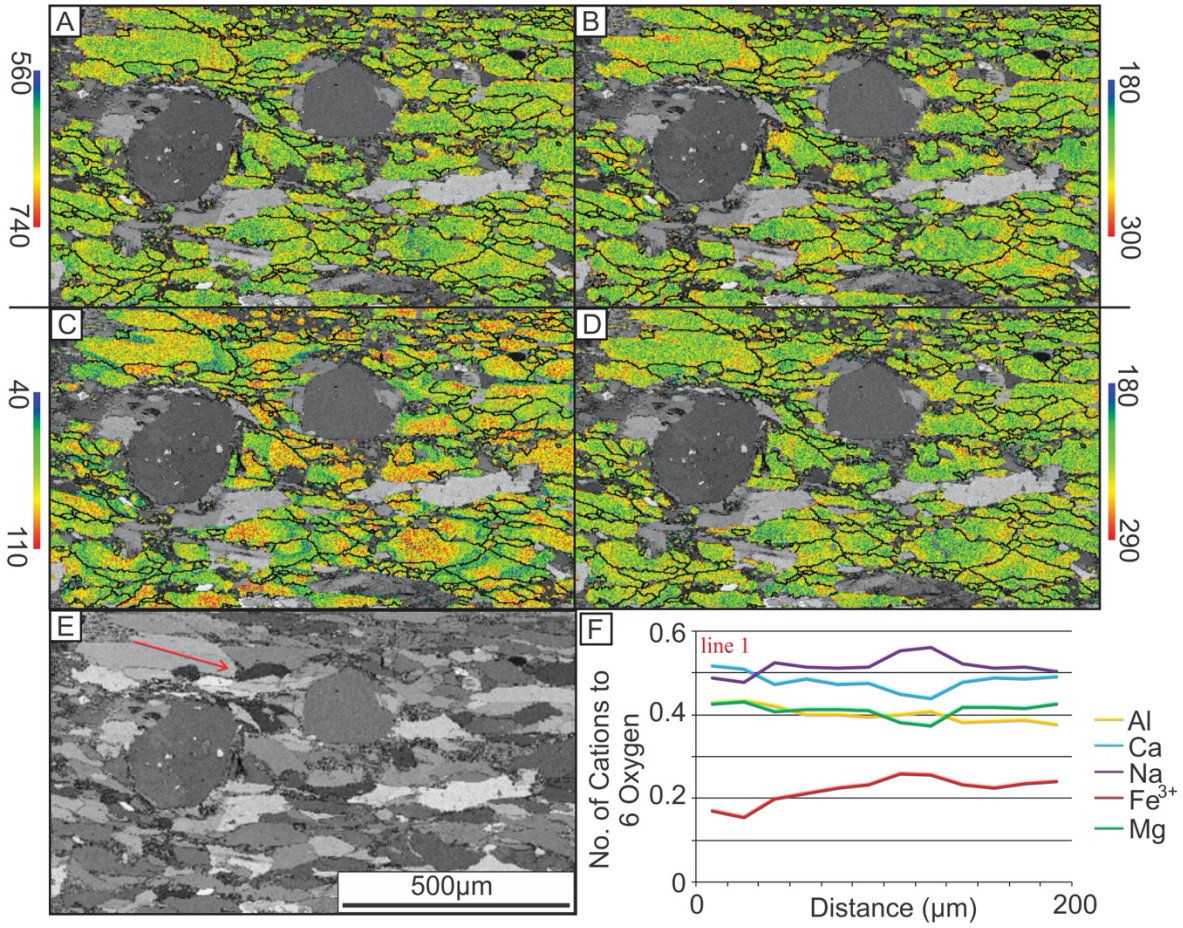

Figure 8. Qualitative EDX chemical maps of omphacite grains (sample S6.8). A) Al counts, B) Ca counts, C) Fe counts, D) Mg counts (data from Camscan X500). E) Backscatter image of the chemical mapped area, red arrow indicates location and direction of quantitative chemical profile shown in, F) graph of number of cations to six oxygen for elements Al, Ca, Na, Fe^{3+}, and Mg along that zoned omphacite grain (data from Cameca SX 100).

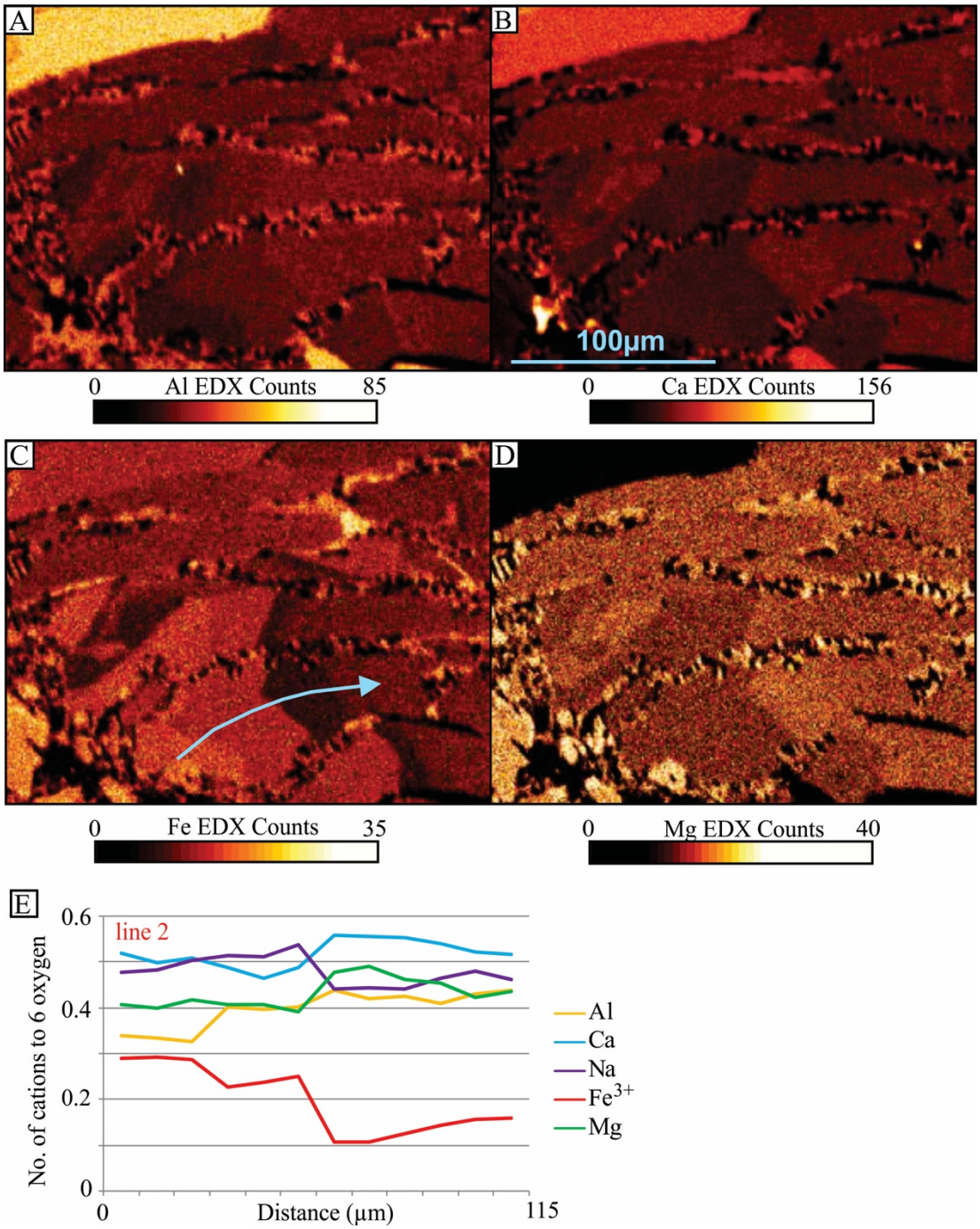

Figure 9. Qualitative EDX chemical maps of omphacite grains (sample S6.13) that show sharp chemical zone boundaries. A) Al counts, B) Ca counts, C) Fe counts, D) Mg counts (data from Camscan X500). E) graph of number of cations to six oxygen for elements Al, Ca, Na, Fe^{3+}, and Mg along a traverse through a zoned omphacite grain (blue arrow in Figure 9c; data from Cameca SX 100, omphacite grain 'omphgraine' in dataset).

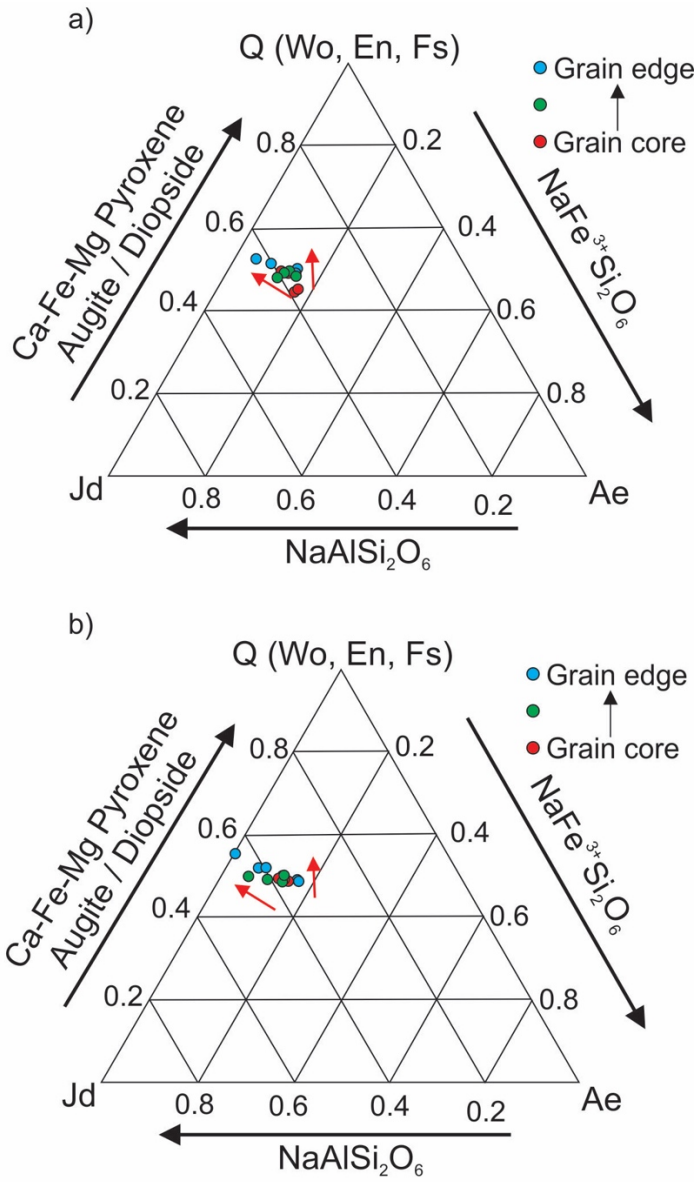

Figure 10. Quad-Jd-Ae pyroxene classification diagram showing the normalised Q (Ca-Fe-Mg pyroxene), Jd (jadeite), and Ae (aegirine) components of two zoned omphacite grains (a and b) from sample S6.8 (Figure 8). Points coloured for location on the grain (core – edge). Red arrows show two chemical trends that the data follows, one the reduction in aegirine component from core to rim and the other a slight increase in the Ca-Fe-Mg pyroxene component (Q) from core to rim. Plot is calculated using the method set out in (Morimoto 1988).

Pseudosection modelling (Figure 11) predicts the observed peak pressure assemblage (glaucophane + omphacite + garnet + muscovite + rutile + epidote + quartz) formed at 580-625 °C and 1.5-2.3 GPa. Retrogression and replacement of glaucophane and omphacite by barroisite occurs at 520-590 °C and 1.1-1.75 GPa.

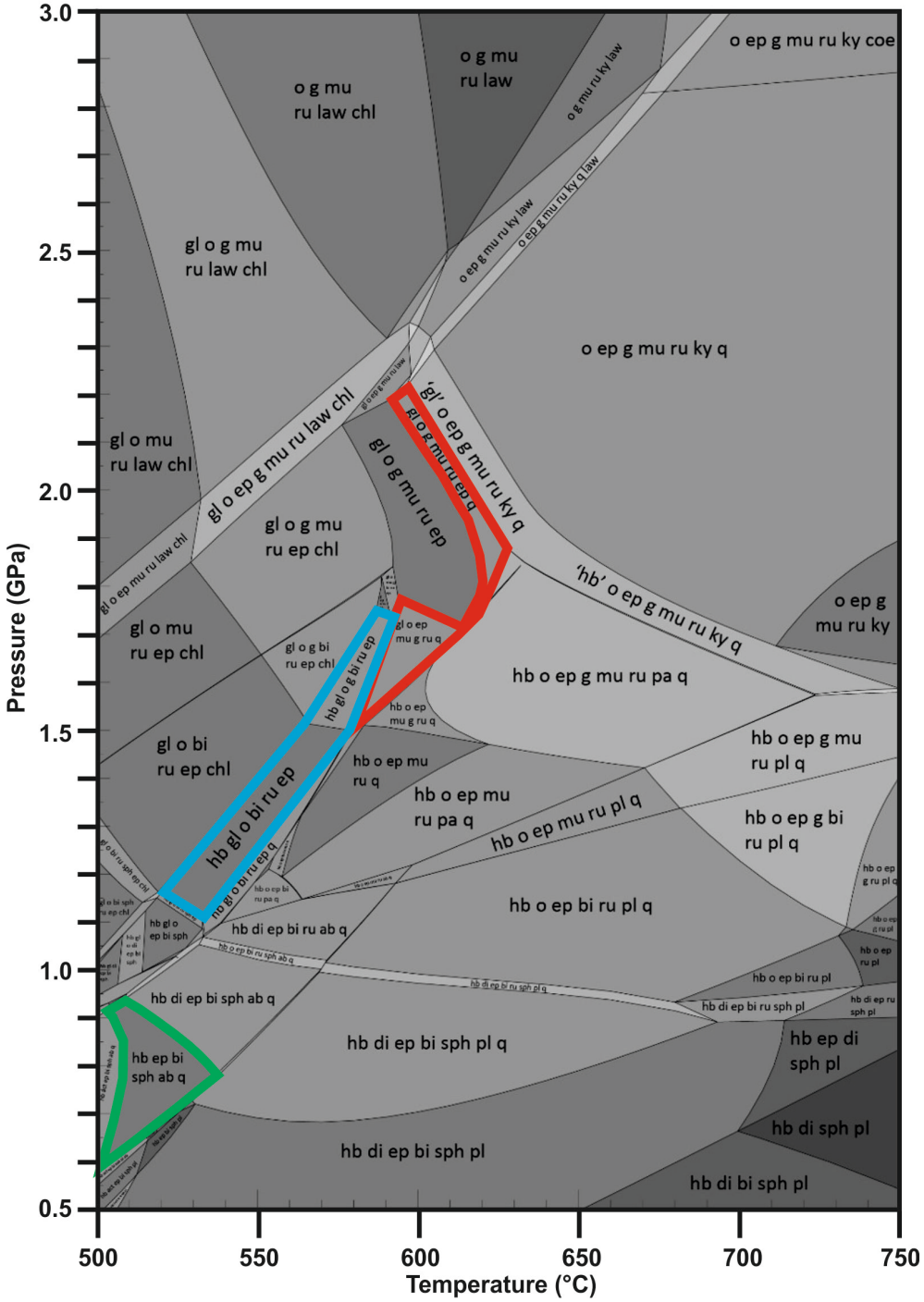

Figure 11. Pseudosection showing mineral phase assemblage pressure-temperature stability fields based on quantitative chemistry and modal abundances of the Punta Telcio eclogites. Red field denotes the range of potential peak-metamorphic conditions, the blue field the range for partially retrogressed conditions, and the green field the fully retrogressed range of conditions of these rocks. (o – omphacite, g – garnet, mu – muscovite, ru – rutile, law – lawsonite, chl – chlorite, gl – glaucophane, ky – kyanite, ep – epidote, q – quartz, coe – coesite, hb – sodic barroisite, bi – biotite, pl – plagioclase, ab – albite, pa – paragonite, di – diopside, sph – sphene, act – actinolite).

512
513 # 4 Discussion
514
515 ## 4.1 Processes responsible for observed omphacite microstructure and
516 microchemistry
517
518 Optical petrography and EBSD grain maps reveal few subgrain boundaries (2°-
519 <10° misorientations), and gradual undulose extinction within omphacite grains,
520 and TEM reveals the rare presence of free dislocations (though not gathered in
521 walls or tangles). In addition, omphacite misorientation distribution analyses
522 show 10-20% omphacite neighbour pair orientation measurements with <10°
523 misorientation angles, indicating some operation of recovery and subgrain
524 rotation and consequently the presence of mobile dislocations (Wheeler et al.
525 2001). We also perform an analysis of omphacite boundary misorientation
526 functions (BMF) for 2°-5° and 5°-10° misorientations (Figure 7) following the
527 process outlined in Rehman et al. (2023). BMF analysis reveals that when
528 omphacite contains subgrain boundaries, some of these display dominant
529 misorientation axes consistent with the action of the [001](100), [001]{110} and
530 ½<110>{110} omphacite slip systems, inferring the action of some dislocation
531 creep in some omphacite grains. No consistent BMF clustering patterns are
532 observed for omphacite between samples though. These observations indicate
533 that omphacite in these eclogitic rocks deformed, at least in part, by dislocation
534 creep which is may contribute to the formation of the observed omphacite
535 LPOs.
536
537 Misorientations between grains in a rock deforming by diffusion creep should
538 not show such microstructures as described above (e.g. albite LPO observed
539 by (Jiang et al. 2000). However, within the omphacite grain in these deformed
540 eclogites there is strong evidence for diffusion creep. This comes from the
541 observation of asymmetric (non-concentric) zoning patterns in individual
542 omphacite grains. Omphacite commonly displays aegirine/jadeite rich cores
543 that zone into more diopsidic omphacite along grain long axes (to either one or
544 both ends), displaying sharp chemical zonation boundaries. These zonation
545 patterns suggest the action of a diffusive mass transfer process, likely Coble

546 creep or pressure solution. We rule out Nabarro-Herring creep as this implies
547 lattice diffusion, which, if active, would smooth the sharp chemical zonation
548 boundaries observed in omphacite here. Omphacite grain sizes for the Punta
549 Telcio eclogites are larger (~250 μm) than those recorded for other phases in
550 other rocks diagnosed as undergoing diffusion creep (e.g. olivine; (Lee et al.
551 2002), and albite; (Jiang et al. 2000). This, however, does not preclude the
552 action of diffusion creep in omphacite here as LPOs are found within omphacite
553 grain sizes up to 7mm that lack evidence for dislocation creep (Mauler et al.
554 2001).
555
556 We propose here that omphacite diffusion creep was occurring as the pressure
557 and temperature experienced by these eclogite rocks underwent retrogression.
558 Omphacite of one composition (jadeite/aegirine) equilibrated at an earlier
559 pressure and temperature and eventually started dissolving at high stress
560 interfaces as deformation of these eclogites progressed. Subsequently, a
561 different omphacite chemistry began precipitating out at low stress interfaces
562 (compositions closer to Ca-Fe-Mg pyroxene – augite/diopside). Growth of
563 richer, Ca-Fe-Mg pyroxene (augite/diopside) around an older core of more
564 jadeite/aegirine composition omphacite may imply this eclogite is undergoing
565 retrogression during the development of this chemical zoning pattern (Tsujimori
566 et al. 2005). This theory is supported by the potential pressure-temperature
567 pathway we establish from pseudosection modelling (Figure 11). Additionally,
568 possible take-up of Na and Fe^{3+} lost from jadeite and aegirine omphacite into
569 retrogressive glaucophane suggests these eclogites are following a
570 retrogressive pathway during this stage of deformation. If we accept this, it
571 suggests that diffusion creep is operating at the latest by the beginning of the
572 exhumation of these eclogites. It follows from this that the operation of
573 dislocation creep, which had to have occurred prior to the formation of the sharp
574 chemical zonation patterns, was an operative deformation mechanism during
575 the eclogites peak pressure and temperature conditions (~580-625 °C, 1.5-2.3
576 GPa), and possibly during the initial retrogression. This explains the sharply
577 defined omphacite chemical zonation patterns observed here. Similar
578 conclusions have been made on the origin of zoning patterns in other mineral
579 phases (Misch 1969; Wintsch and Yi 2002).

Accepting that incongruent pressure solution is occurring like this in omphacite, such that omphacite is only partially dissolving and leaving behind a residual product, other minerals must be involved as reactants and/or products during changing pressure and temperature conditions, or the system was open (Beach 1979; Rutter, 1983). Other minerals within these eclogite rocks show evidence for chemical evolution during deformation. Clinozoisite, throughout most of these deformed eclogites, can also define a shape fabric parallel to that of the omphacite, making it plausible these minerals were deforming/growing at the same time. These foliated clinozoisite crystals can also show non-concentric zonation patterns, like those observed in omphacite (Figure 12a). Fe^{3+} content increases towards the ends of the elongated clinozoisite grains, as shown by higher birefringence (Ackermand and Raase, 1973). Later clinozoisite, not foliated and without an SPO, also shows zonation but without the asymmetrical pattern observed in foliated clinozoisite (Figure 12b). We infer that, like omphacite, clinozoisite is deforming by diffusion creep under changing pressure and temperature conditions, providing a sink for Fe^{3+} that does not enter newly forming omphacite. The reduced Na in omphacite may be explained either by the growth of retrogressive glaucophane during this stage of deformation (McNamara et al. 2012), or by a net transfer reaction producing non-sodic pyroxene components from other phases, hence “diluting” the jadeite component of the deforming omphacite.

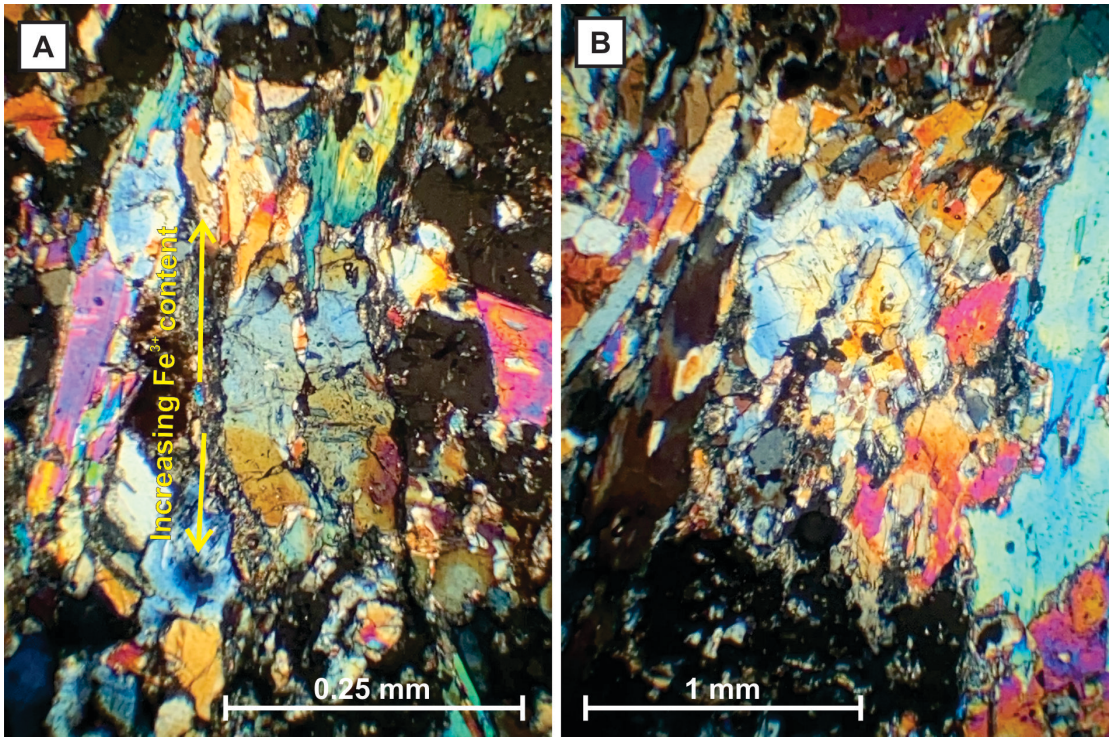

Figure 12. Crossed polarised photomicrographs of eclogite sample S6.14 showing A) asymmetrically zoned finer grained clinozoisite that forms part of the foliation, and B) later stage, larger grained clinozoisite also showing chemical zonation.

4.2 Synthesis

The observed physical and chemical microstructures confirm the action of both dislocation and diffusion creep in the creation of the omphacite LPOs in Punta Telcio eclogites. This agrees with the conclusions of previous works that suggest a combination of deformation mechanisms responsible for omphacite LPO development (Godard and Roermund 1995; Mauler et al. 2001). However, determining whether either of these mechanisms is dominant in omphacite LPO formation, and whether they were operative concurrently, is more difficult. Determining a dominant omphacite deformation mechanism in our samples, if one exists, as well as the sequence that these mechanisms were operating throughout the deformation history of these eclogites, is hindered by the lack of data on the rheology of omphacite, or indeed eclogite rocks themselves. This limits the knowledge of how stress, temperature, and strain rate control the action of various deformation mechanisms in omphacite.

Limited experimental data for pyroxene suggests that it can only flow under high stresses (Jin et al. 2001), yet omphacite in exhumed eclogites often displays evidence for some plastic deformation, as we see in this study of the Punta Telcio eclogites. Information on omphacite rheology is reported from analogue experiments on single crystal diopside (Avé-Lallemant 1978; Ingrin et al. 1992), and polycrystalline omphacite aggregates (Jin et al. 2001; Dimanov et al. 2003). These studies show omphacite deformation by mechanical twinning at low temperature and high strain rates, and a dominance of dislocation creep and diffusion creep at high temperatures. The latter displays some dependence on grain size and flow stresses, suggesting that very high stresses would be required to deform clinopyroxene-rich rocks by dislocation creep under lower crustal or upper mantle conditions (Zhang et al. 2006). This is inconsistent with observations of dislocation creep in omphacite naturally deformed in temperatures as low as 450 °C (Piepenbreier and Stöckhert 2001), and the evidence for dislocation creep in this study's samples (580-625 °C). A possible explanation for this comes from experimental testing of omphacite that indicates it is much weaker than non-sodic pyroxene (Stöckhert and Renner 1998; Jin et al. 2001; Zhang et al. 2006). Experimentally deformed omphacite (strain rates of 10^{-4}–10^{-5}/s, temperatures >1000 °C, confining pressure of 3 GPa) produced typical omphacite LPOs from pure dislocation creep (Zhang et al. 2006), and microstructural observations of ultra-high-pressure jadeite (>900 °C, ≥2.8 GPa) suggest that dislocation creep is the dominant mechanisms at these conditions (Wang et al. 2010). (Zhang et al. 2006) go further to state that due to a lack of evidence in their experiments, or from observation in naturally deformed omphacite of recrystallisation and crystal growth, omphacite LPO forms predominantly from dislocation creep.

This leaves us with an understanding that dislocation creep, sometimes acting alone, can form LPOs in omphacite under the right conditions (>2.8 GPa, >900°C). The deformation P-T of eclogites from the Zermatt-Saas at Punta Telcio do not reach higher than ~2.3 GPa and ~630°C suggesting that dislocation creep would struggle to generate the observed LPOs alone. Further barriers to the action of dislocation creep in omphacite deformation in our samples may be inferred by the presence of antiphase domains. Formation of

antiphase domains in a material can impede dislocation motion though the lattice (Courtney 2005) possibly preventing their organisation into subgrain boundaries, of which few are observed in our samples. In fact studies have suggested that one of the main omphacite dislocations, and ½<110>{$\bar{1}$10}, requires a lot of energy and its action is hindered in omphacite with P2/n structure, supporting the idea that some aspects of dislocation creep is impeded by the formation of antiphase domains in omphacite (Brenker et al. 2002). Finally, the sharp, well-defined chemical zoning patterns observed in these deformed omphacite grains, suggests a minimal amount of dislocation creep activity. If dislocation creep occurred during or after the establishment of these chemical zoning patterns, movement of dislocations, accompanied by recrystallisation and recovery, would have blurred or destroyed them, creating a more diffuse zoning profile. We conclude from our examination of deformed eclogite facies Zermaat-Saas rocks at Punta Telcio, that dislocation creep may have played a minor role in early omphacite deformation, but it is a DMT process, likely preferential dissolution-precipitation that was dominantly responsible for the observable omphacite microstructure in these rocks.

5 Conclusions

- Omphacite in eclogites from the Punta Telcio region of the Zermatt-Saas displays a strong, S-type LPO.
- Rare sub-grain boundaries, undulose extinction, and dislocations and misorientation distribution analysis indicate limited action of dislocation creep in omphacite deformation.
- Asymmetric chemical zoning patterns in omphacite indicate the action of diffusion creep.
- Sharp chemical zonation patterns suggest the diffusion creep acted after dislocation creep.
- The omphacite chemical zonation from aegirine/jadeite cores to Ca-Fe-Mg richer omphacite rims, petrographic observations and textural relationships of omphacite and retrogressive minerals that also define SPO, and asymmetrical chemical zoning in retrogressive minerals

(clinozoisite) indicate diffusion creep happened as these eclogites began to equilibrate under retrogressive conditions during exhumation.

- Microstructures associated with the action of dislocation creep in omphacite, while present in some grains, are uncommon suggesting omphacite LPO is dominantly generated or greatly modified by diffusion creep.

6 Acknowledgements

This research is funded as part of a PhD scholarship provided by the Natural Environmental Research Council (NERC), United Kingdom. The authors would like to thank Professor Wolfgang Müller from the Technische Universität Darmstadt, Germany for his generous contribution to the acquisition and interpretation of the omphacite TEM images presented in this work. Use of Aztec and AztecCrystal software for SEM data analysis is possible thanks to software licences from Oxford Instruments.

7 Data Access

Sample locations, raw EBSD data files in cpr/crc format, and eclogite chemistry data in Excel files are available from Zenodo (McNamara et al., 2023).

8 References

Ábalos B (1997) Omphacite fabric variation in the Cabo Ortegal eclogite (NW Spain): relationships with strain symmetry during high-pressure deformation. J Struct Geol 19:621–637. https://doi.org/10.1016/s0191-8141(97)00001-1

Ackermand D, Raase P (1973) Coexisting zoisite and clinozoisite in biotite schists from the Hohe Tauern, Austria. Contrib Mineral Petr 42:333–341. https://doi.org/10.1007/bf00372611

Amato JM, Johnson CM, Baumgartner LP, Beard BL (1999) Rapid exhumation of the Zermatt-Saas ophiolite deduced from high-precision SmNd and RbSr geochronology. Earth Planet Sc Lett 171:425–438. https://doi.org/10.1016/s0012-821x(99)00161-2

722 Ashby MF (1972) A first report on deformation-mechanism maps. Acta Metall
723 Mater 20:887–897. https://doi.org/10.1016/0001-6160(72)90082-x

724 Atkinson BK (1977) The kinetics of ore deformation: Its illustration and
725 analysis by means of deformation-mechanism maps. Geologiska
726 Foereningan Stock Foerhandlingar 99:186–197.
727 https://doi.org/10.1080/11035897709455013

728 Avé-Lallemant HG (1978) Experimental deformation of diopside and
729 websterite. Tectonophysics 48:1–27. https://doi.org/10.1016/0040-
730 1951(78)90083-5

731 Barnicoat AC, Fry N (1986) High-pressure metamorphism of the Zermatt-
732 Saas ophiolite zone, Switzerland. J Geol Soc London 143:607–618.
733 https://doi.org/10.1144/gsjgs.143.4.0607

734 Bascou J, Barruol G, Vauchez A, Mainprice D (2001) EBSD-measured lattice-
735 preferred orientations and seismic properties of eclogites. Tectonophysics
736 342:61–80. https://doi.org/10.1016/s0040-1951(01)00156-1

737 Bascou J, Tommasi A, Mainprice D (2002) Plastic deformation and
738 development of clinopyroxene lattice preferred orientations in eclogites. J
739 Struct Geol 24:1357–1368. https://doi.org/10.1016/s0191-8141(01)00137-7

740 Beach A (1979) Pressure solution as a metamorphic process in deformed
741 terrigenous sedimentary rocks. Lithos 12:51–58.
742 https://doi.org/10.1016/0024-4937(79)90062-8

743 Blenkinsop T (2002) Deformation Microstructures and Mechanisms in
744 Minerals and Rocks

745 Brenker FE, Müller WF, Brey GP (2003) Variation of antiphase domain size in
746 omphacite: A tool to determine the temperature–time history of eclogites
747 revisited. Am Mineral 88:1300–1311. https://doi.org/10.2138/am-2003-8-
748 912

749 Brenker FE, Prior DJ, Müller WF (2002) Cation ordering in omphacite and
750 effect on deformation mechanism and lattice preferred orientation (LPO). J
751 Struct Geol 24:1991–2005. https://doi.org/10.1016/s0191-8141(02)00010-x

752 Buatier M, Roermund HLM van, Drury MR, Lardeaux JM (1991) Deformation
753 and recrystallization mechanisms in naturally deformed omphacites from
754 the Sesia-Lanzo zone; geophysical consequences. Tectonophysics
755 195:11–27. https://doi.org/10.1016/0040-1951(91)90141-e

756 Bucher K (2005) Blueschists, eclogites, and decompression assemblages of
757 the Zermatt-Saas ophiolite: High-pressure metamorphism of subducted
758 Tethys lithosphere. Am Mineral 90:821–835.
759 https://doi.org/10.2138/am.2005.1718

760 Burov E, Francois T, Agard P, et al (2014) Rheological and geodynamic
761 controls on the mechanisms of subduction and HP/UHP exhumation of
762 crustal rocks during continental collision: Insights from numerical models.
763 Tectonophysics 631:1–39. https://doi.org/10.1016/j.tecto.2014.04.033

764 Cao Y, Du J, Jung H, et al (2021) Crystal preferred orientations, deformation
765 mechanisms and seismic properties of high pressure metamorphic rocks
766 from the Central Qiangtang metamorphic belt, Tibetan Plateau. J Struct
767 Geol 145:104309. https://doi.org/10.1016/j.jsg.2021.104309

768 Carpenter MA (1979) Contrasting properties and behaviour of antiphase
769 domains in pyroxenes. Phys Chem Miner 5:119–131.
770 https://doi.org/10.1007/bf00307548

771 Carpenter MA (1982) Time-temperature-transformation (TTT) analysis of
772 cation disordering in omphacite. Contrib Mineral Petr 78:433–440.
773 https://doi.org/10.1007/bf00375205

774 Clarke JR, Papike JJ (1968) CRYSTAL-CHEMICAL CHARACTERIZATION
775 OF OMPHACITES. THE AMERICAN MINERALOGIST

776 Coggon R, Holland TJB (2002) Mixing properties of phengitic micas and
777 revised garnet-phengite thermobarometers. J Metamorph Geol 20:683–
778 696. https://doi.org/10.1046/j.1525-1314.2002.00395.x

779 Courtney TH (2005) Mechanical behavior of materials. Waveland Press

780 Diener JFA, Powell R, White RW, Holland TJB (2007) A new thermodynamic
781 model for clino- and orthoamphiboles in the system Na2O–CaO–FeO–
782 MgO–Al2O3–SiO2–H2O–O. J Metamorph Geol 25:631–656.
783 https://doi.org/10.1111/j.1525-1314.2007.00720.x

784 Dimanov A, Lavie MP, Dresen G, et al (2003) Creep of polycrystalline
785 anorthite and diopside. J Geophys Res Solid Earth 1978 2012 108:2061.
786 https://doi.org/10.1029/2002jb001815

787 Doin M-P, Henry P (2001) Subduction initiation and continental crust
788 recycling: the roles of rheology and eclogitization. Tectonophysics
789 342:163–191. https://doi.org/10.1016/s0040-1951(01)00161-5

790 Droop GTR (1987) A general equation for estimating Fe 3+ concentrations in
791 ferromagnesian silicates and oxides from microprobe analyses, using
792 stoichiometric criteria. Mineral Mag 51:431–435.
793 https://doi.org/10.1180/minmag.1987.051.361.10

794 Drury MR, Humphreys FJ, White SH (1989) Effect of dynamic recrystallization
795 on the importance of grain-boundary sliding during creep. J Mater Sci
796 24:154–162. https://doi.org/10.1007/bf00660947

797 Erambert M, Austrheim H (1993) The effect of fluid and deformation on zoning
798 and inclusion patterns in poly-metamorphic garnets. Contrib Mineral Petr
799 115:204–214. https://doi.org/10.1007/bf00321220

800 Essene EJ, Fyfe WS (1967) Omphacite in Californian metamorphic rocks.
801 Contrib Mineral Petr 15:1–23. https://doi.org/10.1007/bf01167213

802 Foreman R (2004) The Structural, Microstructural and Metamorphic Evolution
803 of the Drøsdal Eclogite Body, Western Norway. University of Liverpool

804 Godard G, Roermund HLM van (1995) Deformation-induced clinopyroxene
805 fabrics from eclogites. J Struct Geol 17:1425–1443.
806 https://doi.org/10.1016/0191-8141(95)00038-f

807 Green E, Holland T, Powell R (2007) An order-disorder model for omphacitic
808 pyroxenes in the system jadeite-diopsidehedenbergite- acmite, with
809 applications to eclogitic rocks. Am Mineral 92:1181–1189.
810 https://doi.org/10.2138/am.2007.2401

811 Helmstaedt H, Anderson OL, Gavasci AT (1972) Petrofabric studies of
812 eclogite, spinel-Websterite, and spinel-lherzolite Xenoliths from kimberlite-
813 bearing breccia pipes in southeastern Utah and northeastern Arizona. J
814 Geophys Res 77:4350–4365. https://doi.org/10.1029/jb077i023p04350

815 Holland T, Baker J, Powell R (1998) Mixing properties and activity-
816 composition relationships of chlorites in the system MgO-FeO-Al2O3-SiO2-
817 H2O. Eur J Mineral 10:395–406. https://doi.org/10.1127/ejm/10/3/0395

818 Holland T, Powell R (2003) Activity–composition relations for phases in
819 petrological calculations: an asymmetric multicomponent formulation.
820 Contrib Mineral Petr 145:492–501. https://doi.org/10.1007/s00410-003-
821 0464-z

822 Hrstka T, Gottlieb P, Skála R, et al (2018) Automated mineralogy and
823 petrology - applications of TESCAN Integrated Mineral Analyzer (TIMA). J
824 Geosci-czech 47–63. https://doi.org/10.3190/jgeosci.250

825 Ingrin J, Doukhan N, Doukhan J-C (1992) Dislocation glide systems in
826 diopside single crystals deformed at 800-900°C. Eur J Mineral 4:1291–
827 1302. https://doi.org/10.1127/ejm/4/6/1291

828 Jiang Z, Prior DJ, Wheeler J (2000) Albite crystallographic preferred
829 orientation and grain misorientation distribution in a low-grade mylonite:
830 implications for granular flow. J Struct Geol 22:1663–1674.
831 https://doi.org/10.1016/s0191-8141(00)00079-1

832 Jin ZM, ZHANG J, Green HW, Jin S (2001) Eclogite rheology: Implications for
833 subducted lithosphere. Geology 29:667. https://doi.org/10.1130/0091-
834 7613(2001)029<;0667:erifsl>2.0.co;2

835 Karato S-I, Jung H (2003) Effects of pressure on high-temperature dislocation
836 creep in olivine. Philos Mag 83:401–414.
837 https://doi.org/10.1080/0141861021000025829

838 Keppler R (2018) Crystallographic preferred orientations in eclogites – A
839 review. J Struct Geol 115:284–296.
840 https://doi.org/10.1016/j.jsg.2018.04.003

841 Keppler R, Stipp M, Behrmann JH, et al (2016) Deformation inside a
842 paleosubduction channel – Insights from microstructures and
843 crystallographic preferred orientations of eclogites and metasediments
844 from the Tauern Window, Austria. J Struct Geol 82:60–79.
845 https://doi.org/10.1016/j.jsg.2015.11.006

846 Knipe RJ (1989) Deformation mechanisms — recognition from natural
847 tectonites. J Struct Geol 11:127–146. https://doi.org/10.1016/0191-
848 8141(89)90039-4

849 Kurz W, Jansen E, Hundenborn R, et al (2004) Microstructures and
850 crystallographic preferred orientations of omphacite in Alpine eclogites:
851 implications for the exhumation of (ultra-) high-pressure units. J Geodyn
852 37:1–55. https://doi.org/10.1016/j.jog.2003.10.001

853 Lapen TJ, Johnson CM, Baumgartner LP (2003) Burial rates during prograde
854 metamorphism of an ultra-high-pressure terrane: an example from Lago di
855 Cignana, western Alps, Italy. Earth Planet Sc Lett 215:57–72.
856 https://doi.org/10.1016/s0012-821x(03)00455-2

857 Lee K-H, Jiang Z, Karato S (2002) A scanning electron microscope study of
858 the effects of dynamic recrystallization on lattice preferred orientation in
859 olivine. Tectonophysics 351:331–341. https://doi.org/10.1016/s0040-
860 1951(02)00250-0

861 Mainprice D, Bascou J, Cordier P, Tommasi A (2004) Crystal preferred
862 orientations of garnet: comparison between numerical simulations and
863 electron back-scattered diffraction (EBSD) measurements in naturally
864 deformed eclogites. J Struct Geol 26:2089–2102.
865 https://doi.org/10.1016/j.jsg.2004.04.008

866 Mainprice D, Nicolas A (1989) Development of shape and lattice preferred
867 orientations: application to the seismic anisotropy of the lower crust. J
868 Struct Geol 11:175–189. https://doi.org/10.1016/0191-8141(89)90042-4

869 Mauler A, Godard G, Kunze K (2001) Crystallographic fabrics of omphacite,
870 rutile and quartz in Vendée eclogites (Armorican Massif, France).
871 Consequences for deformation mechanisms and regimes. Tectonophysics
872 342:81–112. https://doi.org/10.1016/s0040-1951(01)00157-3

McNamara DD, Wheeler J, Pearce M, Prior D (2023) Punta Telcio Zermatt-Saas Eclogite Mineral Data - Chemistry and Crystallography (Version 1) [Data set]. Zenodo. https://doi.org/10.5281/zenodo.7837199

McNamara DD (2012) Omphacite-a mineral under pressure! Geology Today 28:71–75. https://doi.org/10.1111/j.1365-2451.2012.00830.x

McNamara DD, Wheeler J, Pearce M, Prior DJ (2012) Fabrics produced mimetically during static metamorphism in retrogressed eclogites from the Zermatt-Saas zone, Western Italian Alps. J Struct Geol 44:1–12. https://doi.org/10.1016/j.jsg.2012.08.006

Misch P (1969) Paracrystalline microboudinage of zoned grains and other criteria for synkinematic growth of metamorphic minerals. Am J Sci 267:43–63. https://doi.org/10.2475/ajs.267.1.43

Moghadam RH, Trepmann CA, Stöckhert B, Renner J (2010) Rheology of Synthetic Omphacite Aggregates at High Pressure and High Temperature. J Petrol 51:921–945. https://doi.org/10.1093/petrology/egq006

Morimoto N (1988) Nomenclature of Pyroxenes. Miner Petrol 39:55–76. https://doi.org/10.1007/bf01226262

Müller WF, Brenker FE, Barnert EB, Franz G (2004) Chain multiplicity faults in deformed omphacite from eclogite. Eur J Mineral 16:37–48. https://doi.org/10.1127/0935-1221/2004/0016-0037

Müller WF, Xu Z, Brenker FE (2011) Transmission electron microscopy of omphacite and other minerals in eclogites from the CCSD borehole, China: indications for their deformation and temperature history. Eur J Mineral 23:645–659. https://doi.org/10.1127/0935-1221/2011/0023-2133

Panhuys-Sigler M van, Hartman P (1981) Morphologie théorique de certains pyroxènes déduite de la structure cristalline. Bulletin De Minéralogie 104:95–106. https://doi.org/10.3406/bulmi.1981.7441

Park M, Jung H (2019) Relationships between eclogite - facies mineral assemblages, deformation microstructures, and seismic properties in the Yuka terrane, North Qaidam ultrahigh - pressure metamorphic belt, NW China. J Geophys Res Solid Earth. https://doi.org/10.1029/2019jb018198

Pearce MA, White AJR, Gazley MF (2015) TCInvestigator: automated calculation of mineral mode and composition contours for thermocalc pseudosections. J Metamorph Geol 33:413–425. https://doi.org/10.1111/jmg.12126

Philippot P (1987) “Crack seal” vein geometry in eclogitic rocks. Geodin Acta 1:171–181. https://doi.org/10.1080/09853111.1987.11105136

911 Philippot P, Roermund HLM van (1992) Deformation processes in eclogitic
912 rocks: evidence for the rheological delamination of the oceanic crust in
913 deeper levels of subduction zones. J Struct Geol 14:1059–1077.
914 https://doi.org/10.1016/0191-8141(92)90036-v

915 Piepenbreier D, Stöckhert B (2001) Plastic flow of omphacite in eclogites at
916 temperatures below 500°C - implications for interplate coupling in
917 subduction zones. Int J Earth Sci 90:197–210.
918 https://doi.org/10.1007/s005310000159

919 Prior DJ, Boyle AP, Brenker F, et al (1999) The application of electron
920 backscatter diffraction and orientation contrast imaging in the SEM to
921 textural problems in rocks. Am Mineral 84:1741–1759.
922 https://doi.org/10.2138/am-1999-11-1204

923 Prior DJ, Mariani E, Wheeler J (2009) EBSD in the Earth Sciences:
924 Applications, Common Practice, and Challenges.
925 https://doi.org/10.1007/978-0-387-88136-2 26

926 Prior DJ, Trimby PW, Weber UD, Dingley DJ (1996) Orientation contrast
927 imaging of microstructures in rocks using forescatter detectors in the
928 scanning electron microscope. Mineral Mag 60:859–869.
929 https://doi.org/10.1180/minmag.1996.060.403.01

930 Prior DJ, Wheeler J, Peruzzo L, Spiess R (2002) Some garnet
931 microstructures: an illustration of the potential of orientation maps and
932 misorientation analysis in microstructural studies. J Struct Geol 24:999–
933 1011. https://doi.org/10.1016/s0191-8141(01)00087-6

934 Ranalli G (1982) Deformation maps in grain-size-stress space as a tool to
935 investigate mantle rheology. Phys Earth Planet In 29:42–50.
936 https://doi.org/10.1016/0031-9201(82)90136-4

937 Reddy SM, Wheeler J, Cliff RA (1999) The geometry and timing of orogenic
938 extension: an example from the Western Italian Alps. J Metamorph Geol
939 17:573–589. https://doi.org/10.1046/j.1525-1314.1999.00220.x

940 Rehman HU, Mainprice D, Barou F, et al (2023) Crystallographic preferred
941 orientations and microtexture of the Himalayan eclogites revealing records
942 of syn-deformation peak metamorphic stage and subsequent exhumation.
943 J Struct Geol 167:104792. https://doi.org/10.1016/j.jsg.2023.104792

944 Roermund HLM van (1984) Omphacite Microstructures From a Spanish
945 Eclogite. Texture Stress Microstruct 6:105–116.
946 https://doi.org/10.1155/tsm.6.105

947 Roermund HLM van, Boland JN (1981) The dislocation substructures of
948 naturally deformed omphacites. Tectonophysics 78:403–418.
949 https://doi.org/10.1016/0040-1951(81)90022-6

950 Rogowitz A, Huet B (2021) Evolution of fluid pathways during eclogitization
951 and their impact on formation and deformation of eclogite: A
952 microstructural and petrological investigation at the type locality (Koralpe,
953 Eastern Alps, Austria). Tectonophysics 819:229079.
954 https://doi.org/10.1016/j.tecto.2021.229079

955 Rutter EH (1983) Pressure solution in nature, theory and experiment. J Geol
956 Soc London 140:725–740. https://doi.org/10.1144/gsjgs.140.5.0725

957 Rybacki E, Dresen G (2004) Deformation mechanism maps for feldspar rocks.
958 Tectonophysics 382:173–187. https://doi.org/10.1016/j.tecto.2004.01.006

959 Stöckhert B, Renner J (1998) When Continents Collide: Geodynamics and
960 Geochemistry of Ultrahigh-Pressure Rocks. 57–95.
961 https://doi.org/10.1007/978-94-015-9050-1_3

962 Storey CD, Prior DJ (2005) Plastic Deformation and Recrystallization of
963 Garnet: A Mechanism to Facilitate Diffusion Creep. J Petrol 46:2593–2613.
964 https://doi.org/10.1093/petrology/egi067

965 Stünitz H, Neufeld K, Heilbronner R, et al (2020) Transformation weakening:
966 Diffusion creep in eclogites as a result of interaction of mineral reactions
967 and deformation. J Struct Geol 139:104129.
968 https://doi.org/10.1016/j.jsg.2020.104129

969 Trepmann C, Stöckhert B (2001) Mechanical twinning of jadeite - an indication
970 of synseismic loading beneath the brittle-plastic transition. Int J Earth Sci
971 90:4–13. https://doi.org/10.1007/s005310000165

972 Tsenn MC, Carter NL (1987) Upper limits of power law creep of rocks.
973 Tectonophysics 136:1–26. https://doi.org/10.1016/0040-1951(87)90332-5

974 Tsujimori T, Liou JG, Coleman RG (2005) Coexisting retrograde jadeite and
975 omphacite in a jadeite-bearing lawsonite eclogite from the Motagua Fault
976 Zone, Guatemala. Am Mineral 90:836–842.
977 https://doi.org/10.2138/am.2005.1699

978 Ulrich S, Mainprice D (2004) Does cation ordering in omphacite influence
979 development of lattice-preferred orientation? J Struct Geol 27:419–431.
980 https://doi.org/10.1016/j.jsg.2004.11.003

981 Wang L, Jin ZM, KUSKY T, et al (2010) Microfabric characteristics and
982 rheological significance of ultra-high-pressure metamorphosed jadeite-
983 quartzite and eclogite from Shuanghe, Dabie Mountains, China. J
984 Metamorph Geol 28:163–182. https://doi.org/10.1111/j.1525-
985 1314.2009.00859.x

986 Warren JM, Hirth G (2006) Grain size sensitive deformation mechanisms in
987 naturally deformed peridotites. Earth Planet Sc Lett 248:438–450.
988 https://doi.org/10.1016/j.epsl.2006.06.006

989 Wenk HR, Christie JM (1991) Comments on the interpretation of deformation
990 textures in rocks. J Struct Geol 13:1091–1110.
991 https://doi.org/10.1016/0191-8141(91)90071-p

992 Wheeler J, Prior DJ, Jiang Z, et al (2001) The petrological significance of
993 misorientations between grains. Contrib Mineral Petr 141:109–124.
994 https://doi.org/10.1007/s004100000225

995 White, Powell, Holland, Worley (2000) The effect of TiO2 and Fe2O3 on
996 metapelitic assemblages at greenschist and amphibolite facies conditions:
997 mineral equilibria calculations in the system K2O–FeO–MgO–Al2O3–
998 SiO2–H2O–TiO2–Fe2O3. J Metamorph Geol 18:497–511.
999 https://doi.org/10.1046/j.1525-1314.2000.00269.x

1000 White RW, Powell R, Holland TJB (2007) Progress relating to calculation of
1001 partial melting equilibria for metapelites. J Metamorph Geol 25:511–527.
1002 https://doi.org/10.1111/j.1525-1314.2007.00711.x

1003 White S (1976) The Effects of Strain on the Microstructures, Fabrics, and
1004 Deformation Mechanisms in Quartzites. Philosophical Transactions Royal
1005 Soc Math Phys Eng Sci 283:69–86. https://doi.org/10.1098/rsta.1976.0070

1006 Wintsch RP, Yi K (2002) Dissolution and replacement creep: a significant
1007 deformation mechanism in mid-crustal rocks. J Struct Geol 24:1179–1193.
1008 https://doi.org/10.1016/s0191-8141(01)00100-6

1009 Zhang J, Green HW (2007) Experimental Investigation of Eclogite Rheology
1010 and Its Fabrics at High Temperature and Pressure. J Metamorph Geol
1011 25:97–115. https://doi.org/10.1111/j.1525-1314.2006.00684.x

1012 Zhang J, Green HW, Bozhilov KN (2006) Rheology of omphacite at high
1013 temperature and pressure and significance of its lattice preferred
1014 orientations. Earth Planet Sc Lett 246:432–443.
1015 https://doi.org/10.1016/j.epsl.2006.04.006

1016